Numerical studies of the influence of the dynamic contact angle on a droplet impacting on a dry surface

Kensuke Yokoi,[1,a] Damien Vadillo,[2] John Hinch,[3] and Ian Hutchings[1]
[1]*Institute for Manufacturing, University of Cambridge, Mill Lane, Cambridge CB2 1RX, United Kingdom*
[2]*Department of Chemical Engineering and Biotechnology, University of Cambridge, Pembroke Street, Cambridge CB2 3RA, United Kingdom*
[3]*DAMTP, University of Cambridge, Wilberforce Road, Cambridge CB3 0WA, United Kingdom*

(Received 4 February 2009; accepted 1 June 2009; published online 7 July 2009)

We numerically investigated liquid droplet impact behavior onto a dry and flat surface. The numerical method consists of a coupled level set and volume-of-fluid framework, volume/surface integrated average based multimoment method, and a continuum surface force model. The numerical simulation reproduces the experimentally observed droplet behavior quantitatively, in both the spreading and receding phases, only when we use a dynamic contact angle model based on experimental observations. If we use a sensible simplified dynamic contact angle model, the predicted time dependence of droplet behavior is poorly reproduced. The result shows that precise dynamic contact angle modeling plays an important role in the modeling of droplet impact behavior. © *2009 American Institute of Physics*. [DOI: 10.1063/1.3158468]

I. INTRODUCTION

Droplet impacts onto dry and flat surfaces have been studied by many researchers from both theoretical and practical aspects.[1–19] Droplet impact has many practical applications, for example, in ink-jet printing, fuel injection, and the agrochemical field. Ink-jet technology is now being used not only for printing onto paper but also in the manufacturing process for displays, such as polymer organic light emitting diodes. A recent overview of droplet impact can be found in Ref. 20.

Numerical simulations of droplet impact onto dry surfaces have been conducted by many researchers.[1–9,11,12,15,16,18,19] The numerical methods used in previous work can be categorized into two groups. One is based on fixed grids such as a Cartesian grid.[1–3,6,8,9,11,12,15,16,18,19] The other uses a finite element method (FEM) with moving grid.[5,7] In the fixed grid formulation, the front tracking method,[1,12,21,22] the volume-of-fluid (VOF) method,[23–26] or level set method[27–31] is used to describe liquid interface motion and a finite difference (volume) method is used as fluid solver. The front tracking type method uses Lagrangian objects such as particles to track the liquid interface. The VOF method traces the interface based on the VOF function (volume fraction in each cell) with a geometrical interface reconstruction. The level set method represents the liquid interface by using a contour line of the level set function. An approach using the VOF method as well as the level set method has been widely used for droplet impact simulation. These formulations are relatively easy to implement compared to front tracking approaches. The VOF method and the level set method can easily treat large deformation including topology change in the liquid interface because a fixed grid is used. If a moving mesh is used, the mesh may be twisted depending on the situation and then a special treatment is required. However the interface expression using a moving grid is better than that using a fixed grid. Both approaches have advantages and disadvantages.

In this paper, we employ an approach using a fixed grid and use the coupled level set and volume-of-fluid (CLSVOF) formulation,[32] which uses both the level set method and the VOF method. In this formulation, the VOF method deals with interface motion and the level set method is used for surface tension and wettability computations. In this paper, the tangent of hyperbola for interface capturing/weighed line interface calculation (THINC/WLIC) method[33,34] is used instead of the VOF/piecewise linear interface calculation (PLIC) method.[24–26] Although the THINC/WLIC method is a type of VOF method and satisfies volume conservation, it is easy to implement and the numerical results from the THINC/WLIC method appear to be similar to the results from the VOF/PLIC method. For the flow calculation, we employ a finite volume framework. The constrained interpolation profile-conservative semi-Lagrangian (CIP-CSL) method[35–37] is used as the conservation equation solver. Although finite volume methods usually deal with only the cell average as the variable, the CIP-CSL method uses both the cell average and the boundary value as variables. By using both values (moments), a parabolic interpolation function is constructed in a cell, and the boundary value and the cell average are updated based on the parabolic function. For multidimensional cases, dimensional splitting is used.[38] The volume/surface integrated average based multimoment method (VSIAM3) (Refs. 38 and 39) is a fluid solver which can be combined with the CIP-CSL methods. For the surface tension force, we use the CSF model.[40]

In this paper, we focus on dynamic contact angle. The dynamic contact angle is not well understood and is also difficult to measure. The dynamic contact angle plays an

[a]Author to whom correspondence should be addressed. Telephone: +44 (0)1223 765600. Fax: +44 (0)1223 464217. Electronic mail: ky240@cam.ac.uk and kensuke@kensuke.biz.

important role in not only droplet impact behavior but also various scientific and industrial applications such as splashing,[20,41] biolocomotion,[42–44] and coating. It is known that the surface roughness of the substrate can influence the splash considerably,[20,41] and that the splash can be three dimensional (3D).

There have been several numerical studies of dynamic contact angles. The dynamic contact angle has been considered a function of the triple line velocity. Some simple models are based on a step function using advancing and receding angles[5,16] and some representations use a smoothed step function.[8,11,13] Those models work well for inertia-dominated situations because the velocity dependence of the dynamic contact angle does not appear to be strong.[45] An empirical model[46] for the dynamic contact angle was used in the numerical work by Spelt.[47] This model works for capillary-dominated flows. Another model[48,49] was used in a numerical study by Šikalo *et al.*[15] This model is based on Hoffman's experiments in glass capillary tubes for a wide range of capillary numbers. We have developed a dynamic contact angle model based on droplet impact experiments. Tanner's law[50–54] is used for capillary-dominated situations and experimentally observed constant angles for inertia-dominated situations. Although the same model was used for both spreading and receding in Ref. 15, we use an asymmetric model for spreading and receding. The proposed dynamic contact angle model can quantitatively reproduce droplet impact behavior from impact to steady state, including spreading and recoiling.

In formulations using the VOF method or the level set method, two methodologies have mainly been used to apply the boundary condition of the contact angle. One of those applies the contact angle boundary condition to the normal vectors to the liquid interface at the contact line.[8,15,40] The normal vectors are used for the curvature calculation. The other method extrapolates level set and VOF functions into the solid at the contact line.[9,16,47,55] In this paper, a method by Sussman[55] is used because of its simplicity. In this formulation, we are not even required to find the position of the contact line.

We numerically investigate droplet impact onto a dry and flat surface, for experimental conditions[56] involving a millimeter size droplet of water impacting on a chemically treated silicon wafer. In this experiment, the transient contact angle as well as the contact diameter was measured with high time and spatial resolution by using a high speed camera (resolution 0.1 ms for time and 7 μm for distance). Our numerical simulations used a dynamic contact angle model based on the experiments. The numerical simulations can reproduce the receding phase as well as the spreading phase. We also varied the parameters in the contact angle model. The numerical results show that very precise dynamic contact angle modeling is required to reproduce the droplet behavior quantitatively.

In Sec. II, we briefly describe the experiment. The numerical method and the dynamic contact angle models are described in Secs. III and IV. The numerical results of droplet impact are given in Sec. V.

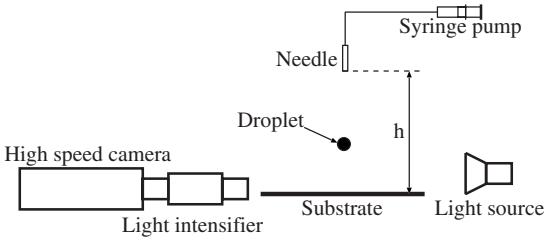

FIG. 1. Schematic figure of the experiment.

II. BRIEF REVIEW OF EXPERIMENT

We briefly describe the experimental method used to measure the contact diameter of the droplet on the substrate and the contact angle.[56] Figure 1 shows a schematic of the experiment. The experimental configuration consists of two parts: the drop generation device and the image recording system. Droplets of several millimeters in diameters are generated with a syringe pump connected to a hypodermic needle 150 μm in diameter. Droplets were formed using the pendant drop method. The method generates a droplet by slowly pushing the liquid through the needle until the drop detaches when its weight overcomes the surface tension. This ensures the repeatability of the droplet size as well as of the impact speed which is acquired under gravity. The distance h between the needle and the surface determines the droplet impact speed. The experimental setup is completed by an optical acquisition system which is combined with adequate drop illumination. It is based on a high speed camera (Nac Memremcam) equipped with a binning option and a 50 W continuous light source. Pictures of 448×338 pixels at a framing rate of 10 000 pictures/s were recorded with a shutter time at 2 μs. In order to increase picture quality and improve edge detection, specifically on the contact line, the camera was combined with a light intensifier which allowed the shutter time to be reduced down to 10 ns. A 200 ns shutter duration was found to give the best compromise between image brightness and edge sharpness. In the experiment, only the right hand side of the droplet was captured to increase the resolution around the triple line.

The recorded surface shape is very sharp and can be easily analyzed using image processing software. As a consequence of the high framing rate, the displacement of the contact line during image acquisition was less than 1 pixel (1 pixel corresponded to 7 μm and the fastest measured velocity of the contact line was 10 m/s). Contact diameter and dynamic contact angle measurements were made by automatic image analysis to ensure accuracy (error $\pm 2\%$ for the diameter and $\pm 3°$ for the contact angle) and avoid human error.

III. NUMERICAL METHOD

A. Interface capturing based on CLSVOF method

In our numerical framework, the interface is tracked by a VOF function evolved by the THINC/WLIC method, and the level set function is constructed based on the interface indicated by the VOF function. Here we should note that VOF methods guarantee conservation when the divergence-free

condition ($\nabla \cdot \mathbf{u}=0$) is precisely satisfied on staggered grids. If the velocity field does not satisfy the divergence-free condition, conservation is not satisfied even though a VOF type method is used.

1. The THINC/WLIC method

The THINC/WLIC method is a type of VOF method. The VOF function is advected by

$$\frac{\partial \chi}{\partial t} + \nabla \cdot (\mathbf{u}\chi) - \chi \nabla \cdot \mathbf{u} = 0. \tag{1}$$

Here $\mathbf{u}$ is the velocity and χ is the characteristic function. The cell average of χ is the VOF function $C_{i,j}$ (axisymmetric case)

$$C_{i,j} = \frac{1}{|\Omega_{i,j}|}\int_{\Omega_{i,j}} \chi r dr dz. \tag{2}$$

The $C_{i,j}$ is evolved by an approximation using a dimensional splitting algorithm as follows:

$$C^*_{i,j} = C^n_{i,j} - \frac{r_{i+1/2,j}F^n_{r,i+1/2,j} - r_{i-1/2,j}F^n_{r,i-1/2,j}}{r_{i,j}\Delta r} + C^n_{i,j}\frac{r_{i+1/2,j}u_{r,i+1/2,j} - r_{i-1/2,j}u_{r,i-1/2,j}}{r_{i,j}\Delta r}\Delta t, \tag{3}$$

$$C^{n+1}_{i,j} = C^*_{i,j} - \frac{F^*_{z,i,j+1/2} - F^*_{z,i,j-1/2}}{\Delta z} + C^n_{i,j}\frac{u_{z,i,j+1/2} - u_{z,i,j-1/2}}{\Delta z}\Delta t, \tag{4}$$

with

$$F_{r,i+1/2,j} = -\int_{z_{i,j-1/2}}^{z_{i,j+1/2}}\int_{r_{i+1/2,j}}^{r_{r,i+1/2,j}-u_{r,i+1/2,j}\Delta t} \chi_{is,j}(r,z) dr dz, \tag{5}$$

$$F_{z,i,j+1/2} = -\int_{z_{i,j+1/2}}^{z_{i,j+1/2}-u_{z,i,j+1/2}\Delta t}\int_{r_{i-1/2,j}}^{r_{i+1/2,j}} \chi_{i,js}(r,z) dr dz. \tag{6}$$

Here $F_{r,i+1/2,j}$ and $F_{z,i,j+1/2}$ are the advection fluxes for the r and z directions, respectively. The is and js are

$$is = \begin{cases} i & \text{if } u_{r,i+1/2,j} \geq 0, \\ i+1 & \text{if } u_{r,i+1/2,j} < 0, \end{cases} \tag{7}$$

and

$$js = \begin{cases} j & \text{if } u_{z,i,j+1/2} \geq 0, \\ j+1 & \text{if } u_{z,i,j+1/2} < 0. \end{cases} \tag{8}$$

The fluxes can be computed by the THINC/WLIC method or the VOF/PLIC method. The details of the THINC/WLIC method used in this paper are given in Refs. 33, 34, and 57. We use the THINC/WLIC method because its implementation is easier than that of the VOF/PLIC method and the results are almost the same.

2. The level set method (CLSVOF)

The level set function ψ (signed distance function) is constructed from the interface indicated by the VOF function by a method[58] which uses the fast marching method[29,59] and an iterative reinitialization scheme proposed by Sussman *et al.*[28] (referred to hereafter as Sussman's method). The level set function ψ within Δh (where Δh is the grid spacing) from the interface indicated by the VOF function is computed by the fast marching method, solving the Eikonal equation

$$|\nabla \psi| = 1. \tag{9}$$

Other ψ further from the interface are calculated by Sussman's method, while ψ computed by the fast marching method is fixed. Sussman's method solves the following problem to a steady state:

$$\frac{\partial \psi}{\partial \tau_1} = S(\psi)(1 - |\nabla \psi|), \tag{10}$$

where τ_1 is artificial time and $S(\psi)$ is a smoothed sign function

$$S(\psi) = \frac{\psi}{\sqrt{\psi^2 + \varepsilon^2}}. \tag{11}$$

To reduce the iteration number of Eq. (10), we also solve the level set equation

$$\frac{\partial \psi}{\partial t} + \mathbf{u} \cdot \nabla \psi = 0, \tag{12}$$

before the calculation of Eq. (10). We just use a first order upwind method for Eq. (12). This is a kind of preconditioner to make ψ^n approach ψ^{n+1}.

The density (color) function ϕ_d which is used to define the physical properties for different materials, such as density and viscosity, can be generated as a smoothed Heaviside function

$$\phi_d = H_\alpha(\psi), \tag{13}$$

with

$$H_\alpha(\psi) = \begin{cases} 0 & \text{if } \psi < -\alpha, \\ \frac{1}{2}\left[1 + \frac{\psi}{\alpha} + \frac{1}{\pi}\sin\left(\frac{\pi\psi}{\alpha}\right)\right] & \text{if } |\psi| \leq \alpha, \\ 1 & \text{if } \psi > \alpha, \end{cases} \tag{14}$$

where 2α represents the thickness of the transition region between the liquid phase and the gas phase. In this paper, $\alpha = \Delta x$ was used. The density function is set as $\phi_d = 1$ for the liquid and $\phi_d = 0$ for the gas. The density ρ and the viscosity coefficient μ are calculated by

$$\rho = \rho_{\text{liquid}}\phi_d + \rho_{\text{air}}(1 - \phi_d), \tag{15}$$

$$\mu = \mu_{\text{liquid}}\phi_d + \mu_{\text{air}}(1 - \phi_d), \tag{16}$$

where ρ_{liquid} and ρ_{air} are the densities of liquid and air, and μ_{liquid} and μ_{air} are the viscosities of liquid and air.

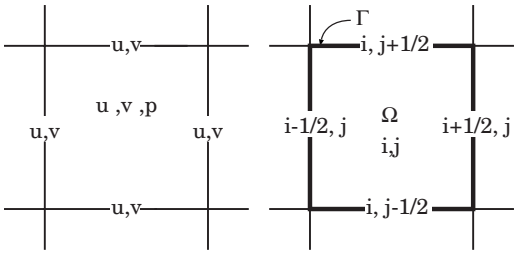

FIG. 2. Grid used in two dimensional case. $u_{i,j}$ is the cell average and $u_{i-1/2,j}$, $u_{i+1/2,j}$, $v_{i,j-1/2}$, and $v_{i,j+1/2}$ are the boundary averages.

B. Governing equations of fluid

We use a finite volume formulation so that we use the following governing equation of an integral form:

$$\int_\Gamma \mathbf{u}\cdot\mathbf{n}dS = 0, \tag{17}$$

$$\frac{\partial}{\partial t}\int_\Omega \mathbf{u}dV + \int_\Gamma \mathbf{u}(\mathbf{u}\cdot\mathbf{n})dS = -\frac{1}{\rho}\int_\Gamma p\mathbf{n}dS + \frac{1}{\rho}\int_\Gamma (2\mu\mathbf{D})\cdot\mathbf{n}dS + \frac{\mathbf{F}_{sf}}{\rho} + \mathbf{g}, \tag{18}$$

where $\mathbf{u}$ is the velocity, $\mathbf{n}$ the outgoing normal vector for the control volume Ω with its surface denoted by Γ (see Fig. 2), ρ is the density, p is the pressure, $\mathbf{D}$ is the deformation tensor $\{\mathbf{D}=0.5[\nabla u+(\nabla u)^T]\}$, $\mathbf{F}_{sf}$ is the surface tension force, and $\mathbf{g}$ is the acceleration due to the gravity. Our formulation is fully conservative for cells not containing the interface, and is only approximately conservative in cells containing the interface. Equations (17) and (18) are solved by a multimoment method based on the CIP-CSL method and VSIAM3.

We use a fractional step approach.[60] Equation (18) is split into three parts as follows:

$$\mathbf{u}^{t+\Delta t} = f^{NA2}\{f^{NA1}[f^{A}(\mathbf{u}^{t})]\}, \tag{19}$$

(1) advection part (f^A),

$$\frac{\partial}{\partial t}\int_\Omega \mathbf{u}dV + \int_\Gamma \mathbf{u}(\mathbf{u}\cdot\mathbf{n})dS = 0, \tag{20}$$

(2) nonadvection part 1 (f^{NA1}),

$$\frac{\partial}{\partial t}\int_\Omega \mathbf{u}dV = \frac{1}{\rho}\int_\Gamma (2\mu\mathbf{D})\cdot\mathbf{n}dS + \frac{\mathbf{F}_{sf}}{\rho} + \mathbf{g}, \tag{21}$$

(3) nonadvection part 2 (f^{NA2}),

$$\int_\Gamma \mathbf{u}\cdot\mathbf{n}dS = 0, \tag{22}$$

$$\frac{\partial}{\partial t}\int_\Omega \mathbf{u}dV = -\frac{1}{\rho}\int_\Gamma p\mathbf{n}dS. \tag{23}$$

The advection part and nonadvection parts are solved by the CIP-CSL method and VSIAM3, respectively.

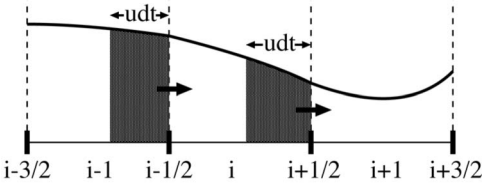

FIG. 3. Schematic of the CIP-CSL method.

C. Grid

We use the grid as shown in Fig. 2. This grid is for a multimoment method (CIP-CSL and VSIAM3) which uses both values of cell averages (or volume integrated average) as well as boundary averages (or surface integrated average).[61] The cell averages $u_{i,j}, v_{i,j}, p_{i,j}$ are defined at the cell center and the boundary averages $u_{i-1/2,j}$, $u_{i,j-1/2}$, $v_{i-1/2,j}$, and $v_{i,j-1/2}$ are defined on the center of the cell boundary. A cell average and a boundary average are both used as variables and these definitions are

$$u_{i,j} = \frac{1}{\Delta r\Delta z}\int_{r_{i-1/2}}^{r_{i+1/2}}\int_{z_{j-1/2}}^{z_{j+1/2}} u(r,z)drdz, \tag{24}$$

$$u_{i-1/2,j} = \frac{1}{\Delta z}\int_{z_{j-1/2}}^{z_{j+1/2}} u(r_{i-1/2},z)dz, \tag{25}$$

$$u_{i,j-1/2} = \frac{1}{\Delta r}\int_{r_{j-1/2}}^{r_{j+1/2}} u(r,z_{j-1/2})dr. \tag{26}$$

D. CIP-CSL method (convection term)

The CIP-CSL method is a solver of the conservation equation

$$\frac{\partial}{\partial t}\int_\Omega \phi dV + \int_\Gamma \phi(\mathbf{u}\cdot\mathbf{n})dS = 0, \tag{27}$$

where ϕ is a scalar value. The CIP-CSL methods have several variations. Here the simplest one, CIP-CSL2 method,[35] is explained. To avoid numerical oscillation, the CIP-CSLR0 method[37] should be used. First we explain the one dimensional case. In the one dimensional case, there are three values (one cell average ϕ_i and two point values $\phi_{i-1/2}$ and $\phi_{i+1/2}$) between $x_{i-1/2}$ and $x_{i+1/2}$. Therefore we can interpolate between $x_{i-1/2}$ and $x_{i+1/2}$ by a quadratic function $\Phi_i(x)$, as shown in Fig. 3,

$$\Phi_i(x) = a_i(x-x_{i-1/2})^2 + b_i(x-x_{i-1/2}) + \phi_{i-1/2}, \tag{28}$$

with

$$a_i = \frac{1}{\Delta x^2}(-6\phi_i + 3\phi_{i-1/2} + 3\phi_{i+1/2}), \tag{29}$$

$$b_i = \frac{1}{\Delta x}(6\phi_i - 4\phi_{i-1/2} - 2\phi_{i+1/2}). \tag{30}$$

By using the interpolation function $\Phi_i(x)$, the boundary value $\phi_{i-1/2}$ is updated by the conservation equation of a differential form

$$\frac{\partial \phi}{\partial t} + u\frac{\partial \phi}{\partial x} = -\phi\frac{\partial u}{\partial x}. \tag{31}$$

A semi-Lagrangian approach is used for Eq. (31),

$$\phi^*_{i-1/2} = \begin{cases} \Phi_{i-1}(x_{i-1/2} - u_{i-1/2}\Delta t) & \text{if } u_{i-1/2} \geq 0, \\ \Phi_i(x_{i-1/2} - u_{i-1/2}\Delta t) & \text{if } u_{i-1/2} < 0, \end{cases} \tag{32}$$

$$\frac{\partial \phi}{\partial t} = -\phi^*\frac{\partial u}{\partial x}. \tag{33}$$

The cell average ϕ_i is updated by a finite volume formulation

$$\frac{\partial}{\partial t}\int_{x_{i-1.2}}^{x_{i+1/2}} \phi dx = -\frac{1}{\Delta x}(F_{i+1/2} - F_{i-1/2}), \tag{34}$$

where $F_{i-1/2}$ is the flux

$$F_{i-1/2} = \begin{cases} -\displaystyle\int_{x_{i-1/2}}^{x_{i-1/2}-u_{i-1/2}\Delta t} \Phi_{i-1}(x)dx & \text{if } u_{i-1/2} \geq 0, \\ -\displaystyle\int_{x_{i-1/2}}^{x_{i-1/2}-u_{i-1/2}\Delta t} \Phi_i(x)dx & \text{if } u_{i-1/2} < 0. \end{cases} \tag{35}$$

For multidimensional cases, a dimensional splitting method[38] is used. In the x-direction computation, $\phi^*_{i,j}$ and $\phi^*_{i-1/2,j}$ are updated based on $\phi^n_{i,j,k}$ and $\phi^n_{i-1/2,j,k}$ by the one dimensional CIP-CSL method. The rest of the values, such as $\phi^n_{i,j-1/2}$, are updated by time evolution converting (TEC) as follows:

$$\phi^*_{i,j-1/2} = \phi^n_{i,j-1/2} + \tfrac{1}{2}(\phi^*_{i,j} - \phi^n_{i,j} + \phi^*_{i,j-1} - \phi^n_{i,j-1}). \tag{36}$$

In axisymmetric geometry, this formulation is little modified. Although we can use the same approach for the z-direction, for the r-directions (31) and (34) must be modified as

$$\frac{\partial \phi}{\partial t} + u\frac{\partial \phi}{\partial r} = -\frac{\phi}{r}\frac{\partial (ru)}{\partial r}, \tag{37}$$

$$\frac{\partial}{\partial t}\int_{r_{i-1.2}}^{r_{i+1/2}} \phi dr = -\frac{1}{r_i \Delta x}(r_{i+1/2}F_{i+1/2} - r_{i-1/2}F_{i-1/2}). \tag{38}$$

E. Viscous stress term

The viscous stress term (39) is discretized by a standard finite volume discretization,[32]

$$\frac{\partial}{\partial t}\int_\Omega \mathbf{u}dV = \frac{1}{\rho}\int_\Gamma (2\mu\mathbf{D})\cdot\mathbf{n}dS. \tag{39}$$

First $\mathbf{u}_{i,j}$ (cell average) is updated. The boundary values such as $u_{i-1/2,j}$ are updated by TEC as explained in the section on the CIP-CSL method (Sec III D).

F. Projection step (pressure gradient term and continuity equation)

By using the divergence of Eq. (23) and $\int_\Gamma \mathbf{u}^{n+1}\cdot\mathbf{n}dS = 0$, the Poisson equation

$$-\int_\Gamma \frac{r}{\rho}\nabla p^{n+1}\cdot\mathbf{n}dS = \frac{1}{\Delta t}\int_\Gamma r\mathbf{u}^*\cdot\mathbf{n}dS \tag{40}$$

is obtained, where $\mathbf{u}^*$ is the velocity after nonadvection step 1. Equation (40) is discretized

$$\begin{aligned} &\frac{\left(\frac{r}{\rho^{n+1}}\partial_r p^{n+1}\right)_{i+1/2,j} - \left(\frac{r}{\rho^{n+1}}\partial_r p^{n+1}\right)_{i-1/2,j}}{\Delta r} \\ &+ \frac{\left(\frac{r}{\rho^{n+1}}\partial_z p^{n+1}\right)_{i,j+1/2} - \left(\frac{r}{\rho^{n+1}}\partial_z p^{n+1}\right)_{i,j-1/2}}{\Delta z} \\ &= \frac{1}{\Delta t}\left(\frac{r_{i+1/2,j}u^*_{i+1/2,j} - r_{i-1/2,j}u^*_{i-1/2,j}}{\Delta r} \right. \\ &\left. + \frac{r_{i,j+1/2}v^*_{i,j+1/2} - r_{i,j-1/2}v^*_{i,j-1/2}}{\Delta z}\right), \end{aligned} \tag{41}$$

where

$$\left(\frac{r}{\rho^{n+1}}\partial_r p^{n+1}\right)_{i-1/2,j} \equiv \frac{2r_{i-1/2,j}}{\rho^{n+1}_{i,j} + \rho^{n+1}_{i-1,j}}\frac{p^{n+1}_{i,j} - p^{n+1}_{i-1,j}}{\Delta r}. \tag{42}$$

A preconditioned BiConjugate Gradient Stabilized (BiCGSTAB) method[62] is used for the pressure Poisson equation. The convergence tolerance of the pressure Poisson equation $\varepsilon_p = 10^{-10}$ is used. This means that the divergence-free condition is precisely satisfied. By using p^{n+1}, the velocity of boundary values ($u_{i-1/2,j}$, $v_{i,j-1/2}$) are updated,

$$u^{n+1}_{i-1/2,j} = u^*_{i-1/2,j} - \left(\frac{1}{\rho^{n+1}}\partial_r p^{n+1}\right)_{i-1/2,j}. \tag{43}$$

Other velocities ($u_{i,j}$, $v_{i,j}$, $u_{i,j-1/2}$, $v_{i-1/2,j}$) are updated by the TEC formula.

G. Model of surface tension force

The surface tension force appears as the surface force

$$\mathbf{F}_{sf} = \sigma\kappa\mathbf{n}_s, \tag{44}$$

where σ is the fluid surface tension coefficient, κ is the local mean curvature, and $\mathbf{n}_s$ is the unit vector normal to the interface. In this calculation, the surface tension force is modeled as a body force $\mathbf{F}_{sf}$ associated with the gradient of the density function

$$\mathbf{F}_{sf} = \sigma\kappa\nabla\phi_d. \tag{45}$$

κ can be computed from

$$\kappa = -\nabla\cdot\mathbf{n}_{ls}. \tag{46}$$

$\mathbf{n}_{ls}$ is evaluated from the level set function

$$\mathbf{n}_{ls} = \frac{\nabla\psi}{|\nabla\psi|}. \tag{47}$$

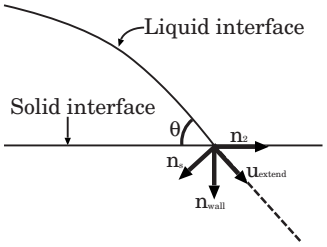

FIG. 4. Contact angle implementation. The dashed line represents the imaginary liquid interface in the solid. The contact angle is taken into account by the imaginary liquid interface represented by the level set function.

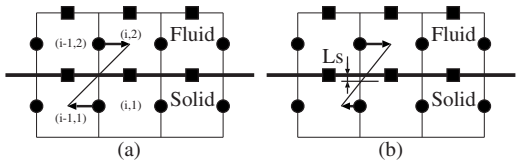

FIG. 5. Schematics no-slip boundary condition (a) and slip length (b). Black circles and squares represent where *r*- and *z*-components of velocity are defined, respectively. The arrow in the fluid represents the velocity of the fluid. The arrow in the solid represents a fictitious velocity to impose the no-slip condition. L_s is the slip length.

H. Contact angle implementation

1. Implementation

To impose the contact angle, we used a method developed by Sussman.[55] An important advantage of this method is that we do not need to locate the position of the triple point in the subgrid explicitly. Contact angle is taken into account by extrapolating the liquid interface represented by the level set function as well as the VOF function into the solid, as shown in Fig. 4.

The liquid interface is extrapolated by solving the extension equation

$$\frac{\partial \psi}{\partial \tau_2} + \mathbf{u}_{\text{extend}} \cdot \nabla \psi = 0, \tag{48}$$

where τ_2 is the artificial time. In this work, $\Delta\tau_2 = 0.5\Delta x$ is chosen. $\mathbf{u}_{\text{extend}}$ is the extension velocity and is computed as follows:

$$\mathbf{u}_{\text{extend}} = \begin{cases} \dfrac{\mathbf{n}_{\text{wall}} - \cot(\pi-\theta)\mathbf{n}_2}{|\mathbf{n}_{\text{wall}} - \cot(\pi-\theta)\mathbf{n}_2|} & \text{if } c < 0, \\ \dfrac{\mathbf{n}_{\text{wall}} + \cot(\pi-\theta))\mathbf{n}_2}{|\mathbf{n}_{\text{wall}} + \cot(\pi-\theta))\mathbf{n}_2|} & \text{if } c > 0, \\ \mathbf{n}_{\text{wall}} & \text{if } c = 0, \end{cases} \tag{49}$$

where

$$\mathbf{n}_{\text{wall}} = (0,-1), \tag{50}$$

$$\mathbf{n}_1 = -\frac{\mathbf{n}_{ls} \times \mathbf{n}_{\text{wall}}}{|\mathbf{n}_{ls} \times \mathbf{n}_{\text{wall}}|}, \tag{51}$$

$$\mathbf{n}_2 = -\frac{\mathbf{n}_1 \times \mathbf{n}_{\text{wall}}}{|\mathbf{n}_1 \times \mathbf{n}_{\text{wall}}|}, \tag{52}$$

$$c = \mathbf{n}_{ls} \cdot \mathbf{n}_2. \tag{53}$$

Here θ is the contact angle. The extension equation is simply solved by using a bilinear interpolation.

2. Singularity at the triple line

In theory, there is a singularity problem at the triple line. If a no-slip condition is imposed on the solid interface the triple line cannot move. However in reality, the triple line does move. In formulations using staggered grids, the singularity problem is avoided. The VOF function which represents the liquid interface is advected by the *r*-component of velocity indicated by the black circles in Fig. 5 and the *z*-component of velocity indicated by the black squares.

Therefore if the *r*-component of velocity has a finite value, the triple line can numerically move. In this formulation, the no-slip condition is imposed by extrapolating the fluid velocity into the solid as the no-slip condition is satisfied,

$$u_{i-1/2,1} = -u_{i-1/2,2}, \tag{54}$$

as shown in Fig. 5(a).[63] This formulation avoids the singularity problem because the *r*-component of velocity is not defined on the solid surface. Additionally the *r*-component of velocity has been defined as the boundary average ($u_{i+1/2,j} = 1/\Delta z \int_{z_{i+1/2,j-1/2}}^{z_{i+1/2,j+1/2}} u dz$). Therefore the *r*-component of velocity can have a finite value and the triple line can numerically move along the solid surface as taking into account the no-slip condition.

In this formula, it is easy to introduce the slip length L_s as

$$u_{i-1/2,1} = \frac{u_{i-1/2,2}}{L_s + \dfrac{\Delta z}{2}} \left(L_s - \frac{\Delta z}{2} \right), \tag{55}$$

as shown in Fig. 5(b). The slip length is used to avoid the singularity problem in formulations which define the velocity on the solid surface such as FEM. In fact a slip length exists in the real world, and has been studied by using molecular dynamics. However, we do not use the concept of slip length because our formulation does not have a singularity problem

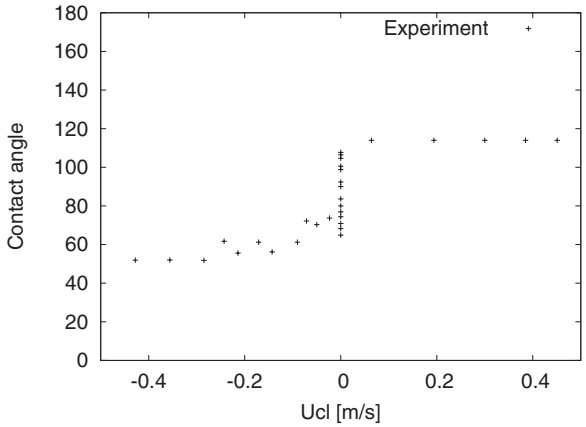

FIG. 6. Experimental measurements of contact angle. The liquid is distilled water and the substrate is a chemically treated silicon wafer. The impact speed is 1 m/s. The droplet diameter is 2.28 mm.

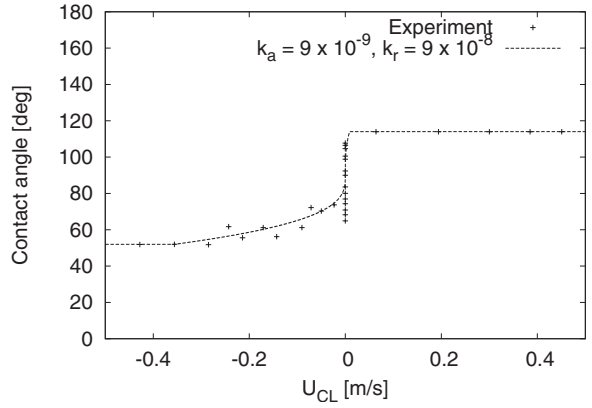

FIG. 7. An approximation to the experimental data (Fig. 6) by Eq. (58). As parameters for the contact angle model, $\theta_{mda}=114°$, $\theta_e=90°$, $\theta_{mdr}=52°$, $k_a=9.0\times10^{-9}$, and $k_r=9.0\times10^{-8}$ are used. The contact angle model is referred as model I.

and we believe that the slip length is much smaller than the mesh size.

IV. DYNAMIC CONTACT ANGLE MODEL

Figure 6 shows the experimental values of contact angle measured during the impact of a 2.28 mm diameter drop arriving at 1 m/s.[56] Here we would like to explain the detail of advancing (receding) contact angles. Two types of advancing (receding) contact angles are experimentally defined: "dynamic" advancing (receding) contact angle and "static" advancing (receding) contact angle. In the droplet impact experiment, the dynamic advancing (receding) contact angle θ_{da} (θ_{dr}) is the angle which is measured during droplet spreading (recoiling). A complex interaction between the fluid viscosity, the surface tension, the inertia, and the substrate results in the dynamic advancing (receding) contact angle being a function of the velocity of the contact line U_{CL}. In the measurements, the dynamic advancing (receding) contact angle tends to a limit as U_{CL} increases (decreases), as shown in Fig. 6. We name these limits the maximum dynamic advancing angle (θ_{mda}) and the minimum dynamic receding angle (θ_{mdr}).

In contrast, the static advancing (receding) contact angle θ_{sa} (θ_{sr}) is defined as the maximum (minimum) angle observed when the triple line speed is zero or nearly zero (i.e., quasistatic).[45]

We propose a dynamic contact angle model. The model is based on Tanner's law[50–54]

$$\mathrm{Ca} = k(\theta_d - \theta_e)^3, \tag{56}$$

for capillary-dominated situation (low Ca number), where Ca is the Capillary number ($\mathrm{Ca} \equiv \mu U_{CL}/\sigma$) and k is a material-related constant which is empirically determined. The angles θ_d and θ_e are the dynamic contact angle and the equilibrium contact angle, respectively. Another approximation is used for the inertia-dominated situation. When inertia is dominant (high Ca number), the constant angles, θ_{mda} and θ_{mdr}, are used

$$\theta_d(U_{CL}) = \begin{cases} \theta_{mda} & \text{if } U_{CL} > 0, \\ \theta_{mdr} & \text{if } U_{CL} < 0, \end{cases} \tag{57}$$

as shown in Fig. 6. The proposed model is based on Eqs. (56) and (57).

The dynamic contact angle model simply consists of Eqs. (56) and (57) as

$$\theta(U_{CL}) = \begin{cases} \min\left[\theta_e + \left(\dfrac{\mathrm{Ca}}{k_a}\right)^{1/3}, \theta_{mda}\right] & \text{if } U_{CL} \geq 0, \\ \max\left[\theta_e + \left(\dfrac{Ca}{k_r}\right)^{1/3}, \theta_{mdr}\right] & \text{if } U_{CL} < 0, \end{cases} \tag{58}$$

where k_a and k_r are material-related parameters for advancing and receding, respectively. These parameters k_a and k_r are determined as the best fit parameters to the measurement

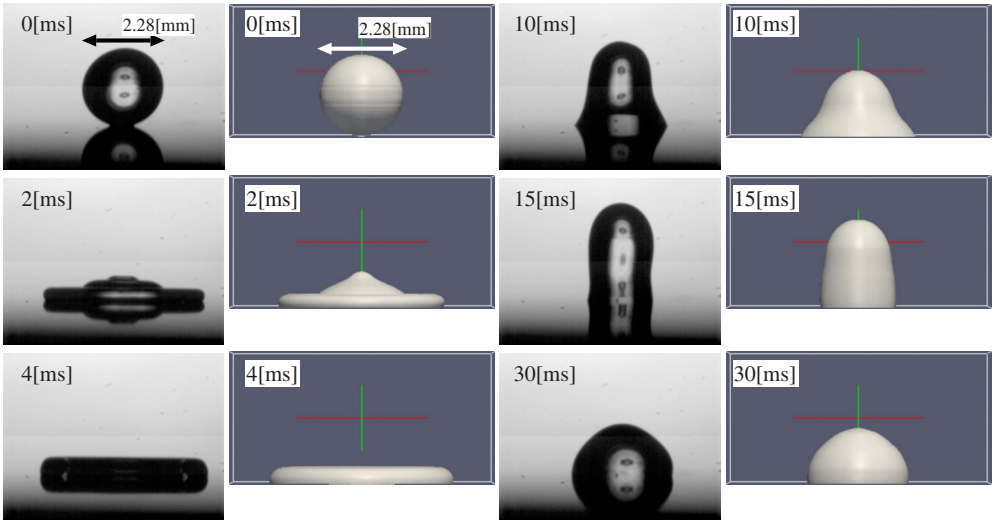

FIG. 8. (Color online) Comparison of appearance between the experimental and numerical results for model I. The left and right hand sides are experimental and numerical results, respectively. Although the numerical results appear 3D, the simulation is two dimensional. The grid size is 100×100. The snapshots were not obtained from the same experiment in which the dynamic contact angle and the diameter were measured, although the conditions are as similar as possible. This is because the experiment to measure contact angle and diameter captures only the right hand side of the droplet in order to increase the resolution around the triple line (enhanced online). [URL: http://dx.doi.org/10.1063/1.3158468.1], [URL: http://dx.doi.org/10.1063/1.3158468.2]

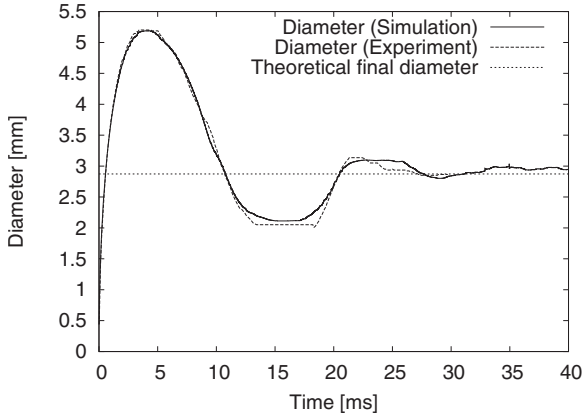

FIG. 9. Time evolution of droplet diameter (contact patch diameter) for model I.

(Fig. 6). We assumed that if $\theta_{\mathrm{mdr}} < \theta_d < \theta_{\mathrm{mda}}$, the system is in the capillary phase, and Tanner's law (56) is used. If the contact angle reached θ_{mda} or θ_{mdr}, we considered that it was no longer in the capillary phase and applying the other law (57). Figure 7 compares a result of Eq. (58) to the experimental data.

V. NUMERICAL RESULTS

We performed axisymmetric simulations of droplet impact onto a dry surface. We used the densities $\rho_{\mathrm{liquid}} = 1000\ \mathrm{kg/m^3}$, $\rho_{\mathrm{air}} = 1.25\ \mathrm{kg/m^3}$, viscosities $\mu_{\mathrm{liquid}} = 1.0 \times 10^{-3}$ Pa s, $\mu_{\mathrm{air}} = 1.82 \times 10^{-5}$ Pa s, surface tension $\sigma = 7.2 \times 10^{-2}$ N/m, gravity 9.8 $\mathrm{m/s^2}$, initial droplet diameter $D = 2.28$ mm, and impact speed 1 m/s. The liquid was distilled water. The substrate was a silicon wafer onto which hydrophobic silane has been grafted using standard microelectronic procedures. The surface roughness is less than 50 nm. The equilibrium contact angle of the substrate with distilled water is 90°. The static advancing and receding contact angles are 107° and 77°, respectively. The static angles were measured with a goniometer.

Figure 8 shows snapshots of comparisons between the numerical results from the dynamic contact angle model of Fig. 7 (hereafter referred to as model I) and the experiment.

Only the right hand side from the center of the droplet is computed. The grid size is 100×100. Figure 9 shows the numerical result for time evolution of the contact patch diameter on the substrate. The numerical result using model I shows good agreement with the experiment. The Appendix shows numerical results using different grid sizes.

To study the importance of using appropriate contact angles, we conducted a numerical simulation using only the equilibrium contact angle (hereafter referred to as model II). instead of the dynamic contact angle model. Figures 10 and 11 show snapshots of the numerical results and the time evolution of the diameter, respectively. This result shows that numerical simulation using the equilibrium contact angle (model II) is not suitable. Even partial rebound is observed. This simulation overestimates the maximum diameter because the dynamic advancing contact angle is underestimated during spreading (i.e., the dissipation of the inertia is under-

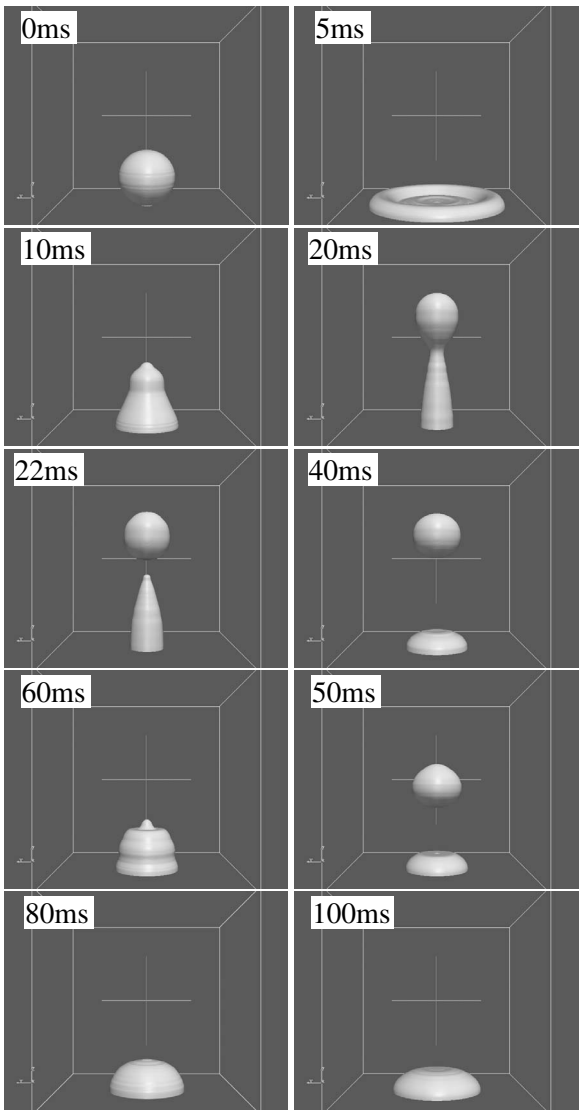

FIG. 10. Snapshots of numerical result obtained using the equilibrium contact angle (model II) (enhanced online). [URL: http://dx.doi.org/10.1063/1.3158468.3]

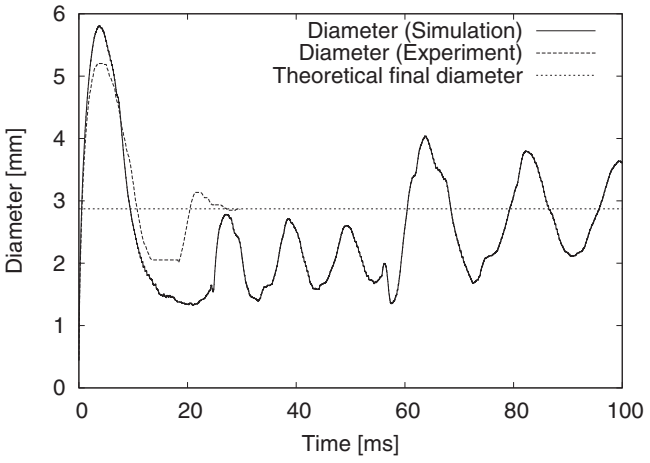

FIG. 11. Time evolution of droplet diameter when the equilibrium angle (model II) is used instead of the dynamic contact angle model.

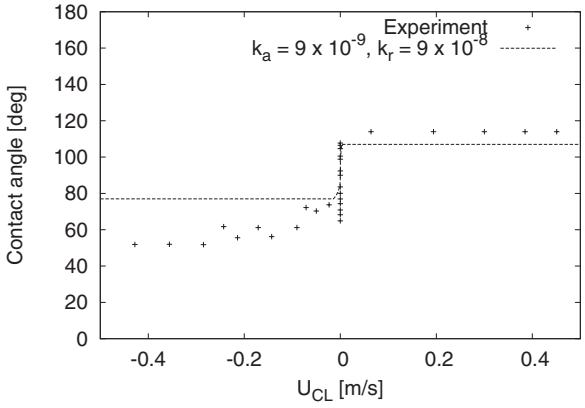

FIG. 12. The dynamic contact angle model using the static advancing and receding contact angles (model III) instead of dynamic advancing and receding contact angles. As parameters of the contact angle model, $\theta_{mda}=107°$, $\theta_e=90°$, $\theta_{mdr}=77°$, $k_a=9.0\times10^{-9}$, and $k_r=9.0\times10^{-8}$ are used.

estimated). For retreating, the receding contact angle is overestimated. If the contact angle is overestimated during recoil, the contact angle cannot reduce the speed of the contact line sufficiently. As a result, the triple line retreats too far. The dynamic contact angle usually reduces the speed of the triple line. However if only 90° equilibrium angle is used, the contact angle does not reduce the triple line speed, and therefore the diameter does not stabilize even after 100 ms.

We conducted a numerical simulation using the static advancing and receding contact angles (model III), instead of the maximum dynamic advancing contact angle and the minimum dynamic receding contact angle, as shown in Fig. 12. Figures 13 and 14 show snapshots of the numerical results and time evolution of the diameter, respectively. The numerical results show that the behavior is different from the experiment (shown in Fig. 8). However the numerical results may be better than those using the equilibrium angle (model II). During impact and spreading, the deviation is not so great because the substrate is hydrophobic, and therefore θ_{mda} and θ_{sa} are close. The maximum diameter is slightly overshot because the static advancing contact angle is little lower than the actual dynamic advancing contact angle. However, retreating gives a large error in terms of appearance as well as in the diameter prediction. This is because the receding contact angle is considerably overestimated, as in the simulation using the equilibrium angle (model II). This result shows that numerical simulation using static angles (model III) is also not suitable.

To study the importance of using appropriate θ_{mda} and θ_{mdr}, we conducted a numerical simulation using 175° and 5° instead of the measured maximum dynamic advancing and minimum receding contact angles, respectively. Figure 15 shows this dynamic contact angle model (model IV) and Fig. 16 shows the numerical result. The maximum diameter is underestimated because the dynamic advancing contact angle is overestimated, as shown in Fig. 15. This numerical result shows that using appropriate θ_{mda} and θ_{mdr} is important.

To study the influences of smoothing in the dynamic contact angle model, we conducted numerical simulations

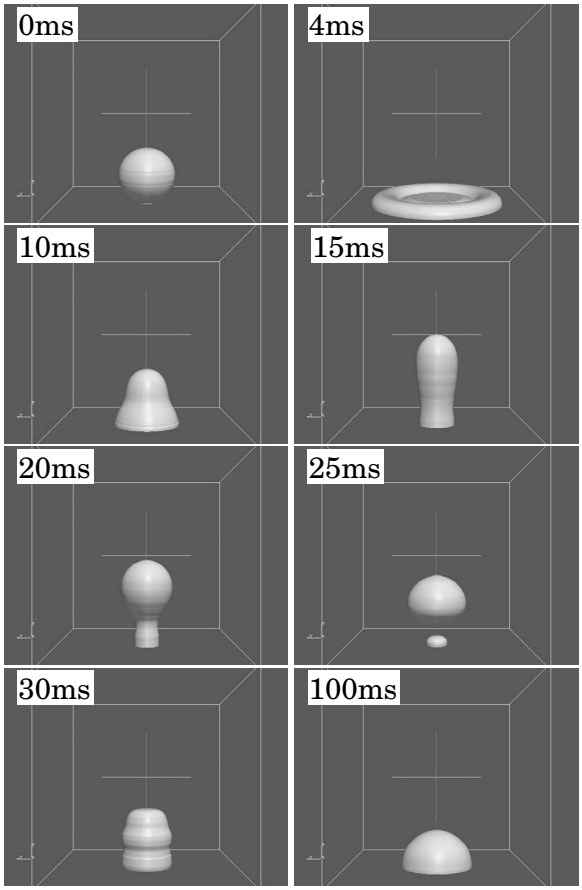

FIG. 13. Snapshots of the numerical result using model III (enhanced online). [URL: http://dx.doi.org/10.1063/1.3158468.4]

using a sharp dynamic contact angle model (model V) using $k_a=9\times10^{-9}$ and $k_r=9\times10^{-9}$, as shown in Fig. 17. Figure 18 shows the numerical result from model V. During impact and spreading, including the maximum diameter prediction, the numerical result shows good agreement. This is because the sharp contact angle model (model V) for advancing ($U_{CL}\geq0$) is the same as that of model I. However the result for the recoil phase does not agree quantitatively with experiment because the contact angle is underestimated in $-0.2<U_{CL}<0$. The underestimated contact angle reduces recoil.

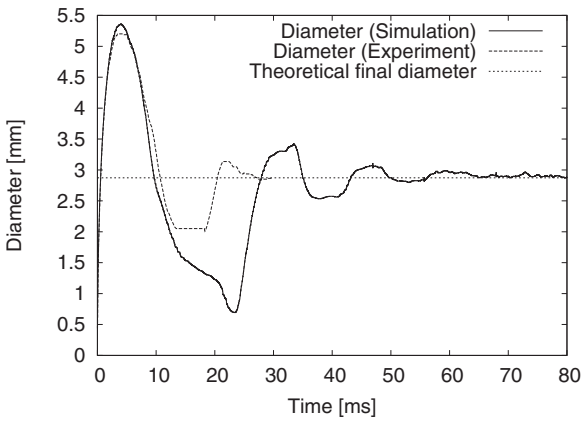

FIG. 14. Time evolution of droplet diameter when model III is used.

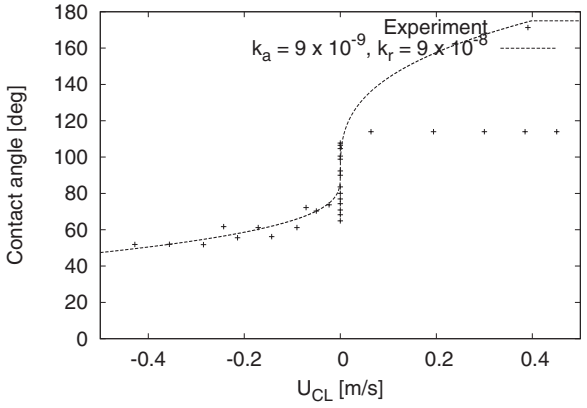

FIG. 15. The dynamic contact angle model (model IV) using $\theta_{mda}=175°$, $\theta_{mdr}=5°$, $k_a=9.0\times10^{-9}$, and $k_r=9.0\times10^{-8}$.

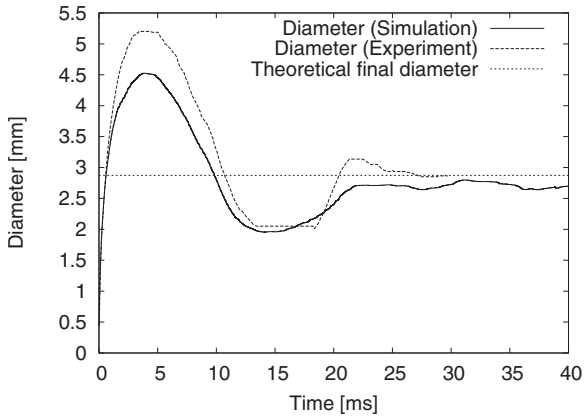

FIG. 16. Time evolution of droplet diameter when model IV is used.

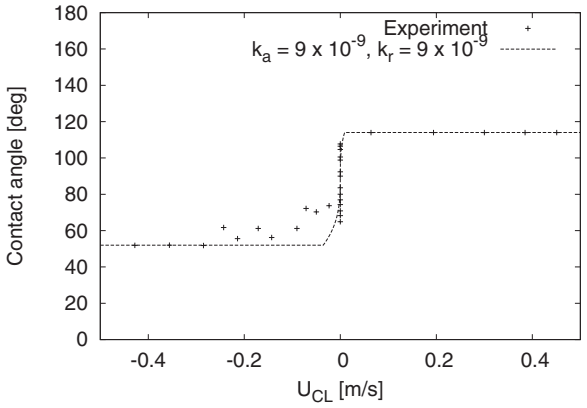

FIG. 17. Sharp dynamic contact angle model (model V). $\theta_{mda}=114°$, $\theta_e=90°$, $\theta_{mdr}=52°$, $k_a=9\times10^{-9}$, and $k_r=9\times10^{-9}$ are used.

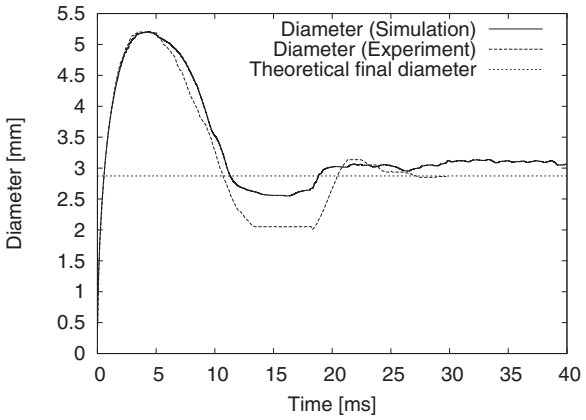

FIG. 18. Time evolution of droplet diameter using model V.

As a result, the numerical simulation did not achieve a metastable diameter in the time period of 13–18 ms (Fig. 18).

VI. CONCLUSIONS

We conducted axisymmetric simulations for droplet impact onto a dry plane surface. Our numerical formulation can robustly simulate droplet impact behavior. We introduced a dynamic contact angle model based on the experimental measurement. To approximate the measured values of dynamic contact angle, we used Tanner's law for low Ca number, the maximum dynamic advancing angle and the minimum dynamic receding angle for high Ca number, and the equilibrium contact angle for Ca=0.

Our numerical results show that using appropriate maximum and minimum angles, and smoothing of the dynamic contact angle model are important. Numerical results of model II (using equilibrium angle) and model III (using static angles) showed totally different behavior from the experiment. Numerical results using different maximum/minimum dynamic angles (model IV) and smoothing (model V) did not show good agreement with the experiment, either.

The contact angle model is asymmetric in terms of amplitudes as well as smoothing, such as the experimental measurement. The asymmetric dynamic contact angle model is important in predicting precisely not only the advancing phase but also the receding phase of drop impact.

ACKNOWLEDGMENTS

Numerical computations in this work were partially carried out on SX8 at the Yukawa Institute for Theoretical Physics, Kyoto University. The experiment was carried out while D.V. was at Laboratoire des Ecoulements Géophysiques et Industriels, University Joseph Fourier. D.V. acknowledges financial support from the MENRT through Project No. Σ 2911. We acknowledge the support of the EPSRC.

APPENDIX: RESOLUTION STUDY

Figure 19 shows the numerical results obtained with three different grid sizes (50×50, 100×100, and 200×200, respectively) with the parameters of the model held fixed. The results are close. In particular the final diameter

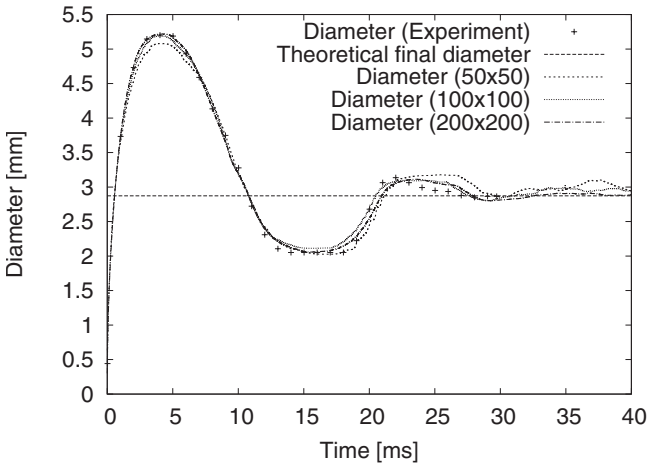

FIG. 19. Time evolution of droplet diameter using 50×50, 100×100, and 200×200 grid resolutions. The experimental data are plotted as "+" to avoid cluttering the figure.

and the time of the first rebound are insensitive to the resolution. We are therefore confident that the 100×100 grid used in this article is sufficiently accurate, while costing $\frac{1}{16}$th that of the 200×200 grid.

[1]F. H. Harlow and J. P. Shannon, "The splash of a liquid drop," J. Appl. Phys. **38**, 3855 (1967).
[2]K. Tsurutani, M. Yao, J. Senda, and H. Fujimoto, "Numerical analysis of the deformation process of a droplet impinging upon a wall," JSME Int. J., Ser. II **33**, 555 (1990).
[3]G. Trapaga and J. Szekely, "Mathematical modeling of the isothermal impingement of liquid droplets in spraying processes," Metall. Trans. B **22**, 901 (1991).
[4]Y. D. Shikhmurzaev, "The moving contact line on a smooth solid surface," Int. J. Multiphase Flow **19**, 589 (1993).
[5]J. Fukai, Z. Zhao, D. Poulikakos, C. M. Megaridis, and O. Miyatake, "Modeling of the deformation of a liquid droplet impinging upon a flat surface," Phys. Fluids A **5**, 2588 (1993).
[6]A. Karl, K. Anders, M. Rieber, and A. Frohn, "Deformation of liquid droplets during collisions with hot walls: Experiment and numerical results," Part. Part. Syst. Charact. **13**, 186 (1996).
[7]M. Bertagnolli, M. Marchese, G. Jacucci, I. St. Doltsinis, and S. Noelting, "Thermomechanical simulation of the splashing of ceramic droplets on a rigid substrate," J. Comput. Phys. **133**, 205 (1997).
[8]M. Bussmann, S. Chandra, and J. Mostaghimi, "Modeling the splash of a droplet impacting a solid surface," Phys. Fluids **12**, 3121 (2000).
[9]M. Renardy, Y. Renardy, and J. Li, "Numerical simulation of moving contact line problems using a volume-of-fluid method," J. Comput. Phys. **171**, 243 (2001).
[10]R. Rioboo, M. Marengo, and C. Tropea, "Time evolution of liquid drop impact onto solid, dry surfaces," Exp. Fluids **33**, 112 (2002).
[11]M. Pasandideh-Fard, S. Chandra, and J. Mostaghimi, "A three-dimensional model of droplet impact and solidification," Int. J. Heat Mass Transfer **45**, 2229 (2002).
[12]Y. Renardy, S. Popinet, L. Duchemin, M. Renardy, S. Zaleski, C. Josserand, M. A. Drumwright-Clarke, D. Richard, C. Clanet, and D. Quere, "Pyramidal and toroidal water drops after impact on a solid surface," J. Fluid Mech. **484**, 69 (2003).
[13]M. Francois and W. Shyy, "Computations of drop dynamics with the immersed boundary method. Part 2. Drop impact and heat transfer," Numer. Heat Transfer, Part B **44**, 119 (2003).
[14]D. C. D. Roux and J. J. Cooper-White, "Dynamics of water spreading on a glass surface," J. Colloid Interface Sci. **277**, 424 (2004).
[15]S. Sikalo, H.-D. Wilhelm, I. V. Roisman, S. Jakirli, and C. Tropea, Dynamic contact angle of spreading droplets: Experiments and simulations," Phys. Fluids **17**, 062103 (2005).
[16]H. Liu, S. Krishnan, S. Marella, and H. S. Udaykumar, "Sharp interface Cartesian grid method II: A technique for simulating droplet interactions with surfaces of arbitrary shape," J. Comput. Phys. **210**, 32 (2005).
[17]I. S. Bayer and C. M. Megaridis, "Contact angle dynamics in droplets impacting on flat surfaces with different wetting characteristics," J. Fluid Mech. **558**, 415 (2006).
[18]H. Ding and P. D. M. Spelt, "Inertial effects in droplet spreading: A comparison between diffuse-interface and level-set simulations," J. Fluid Mech. **576**, 287 (2007).
[19]S. A. Zakerzadeh, "Applying dynamic contact angles to a three-dimensional VOF model," Ph.D. thesis, University of Toronto, 2008.
[20]A. L. Yarin, "Drop impact dynamics: Splashing, spreading, receding, bouncing," Annu. Rev. Fluid Mech. **38**, 159 (2006).
[21]S. O. Unverdi and G. Tryggvason, "A front tracking method for viscous, incompressible multi-fluid flow," J. Comput. Phys. **100**, 25 (1992).
[22]S. Popinet and S. Zaleski, "Bubble collapse near a solid boundary: A numerical study of the influence of viscosity," J. Fluid Mech. **464**, 137 (2002).
[23]C. W. Hirt and B. D. Nichols, "Volume of fluid (VOF) methods for the dynamic of free boundaries," J. Comput. Phys. **39**, 201 (1981).
[24]D. L. Youngs, "Time-dependent multi-material flow with large fluid distortion," in *Numerical Methods for Fluid Dynamics*, edited by K. W. Morton and M. J. Baines (Academic, New York, 1982), Vol. 24, pp. 273–285.
[25]J. Li, "Calcul d'interface affine par Morceaux (piecewise linear interface calculation)," Acad. Sci., Paris, C. R. **320**, 391 (1995).
[26]R. Scardovelli and S. Zaleski, "Direct numerical simulation of free-surface and interfacial flow," Annu. Rev. Fluid Mech. **31**, 567 (1999).
[27]S. Osher and J. A. Sethian, "Front propagating with curvature-dependent speed: Algorithms based on Hamilton-Jacobi formulation," J. Comput. Phys. **79**, 12 (1988).
[28]M. Sussman, P. Smereka, and S. Osher, "A level set approach for capturing solution to incompressible two-phase flow," J. Comput. Phys. **114**, 146 (1994).
[29]J. A. Sethian, *Level Set Methods and Fast Marching Methods* (Cambridge University Press, Cambridge, 1999).
[30]S. Osher and R. Fedkiw, "Level set methods and dynamic implicit surfaces," *Applied Mathematical Sciences* (Springer-Verlag, New York, 2003), No. 153.
[31]K. Yokoi and F. Xiao, "Mechanism of structure formation in circular hydraulic jumps: Numerical studies of strongly deformed free surface shallow flows," Physica D **161**, 202 (2002).
[32]M. Sussman and E. G. Puckett, "A coupled level set and volume-of-fluid method for computing 3D and axisymmetric incompressible two-phase flows," J. Comput. Phys. **162**, 301 (2000).
[33]K. Yokoi, "Efficient implementation of THINC scheme: A simple and practical smoothed VOF algorithm," J. Comput. Phys. **226**, 1985 (2007).
[34]K. Yokoi, "A numerical method for free-surface flows and its application to droplet impact on a thin liquid layer," J. Sci. Comput. **35**, 372 (2008).
[35]T. Yabe, R. Tanaka, T. Nakamura, and F. Xiao, "An exactly conservative semi-Lagrangian scheme (CIP-CSL) in one dimension," Mon. Weather Rev. **129**, 332 (2001).
[36]T. Yabe, F. Xiao, and T. Utsumi, "Constrained interpolation profile method for multiphase analysis," J. Comput. Phys. **169**, 556 (2001).
[37]F. Xiao, T. Yabe, X. Peng, and H. Kobayashi, "Conservative and oscillation-less atmospheric transport schemes based on rational functions," J. Geophys. Res. **107**, 4609 (2002).
[38]F. Xiao, A. Ikebata, and T. Hasegawa, "Numerical simulations of free-interface fluids by a multi integrated moment method," Comput. Struct. **83**, 409 (2005).
[39]F. Xiao, R. Akoh, and S. Ii, "Unified formulation for compressible and incompressible flows by using multi integrated moments II: Multi-dimensional version for compressible and incompressible flows," J. Comput. Phys. **213**, 31 (2006).
[40]J. U. Brackbill, D. B. Kothe, and C. Zemach, "A continuum method for modeling surface tension," J. Comput. Phys. **100**, 335 (1992).
[41]P. Tsai, S. Pacheco, C. Pirat, L. Lefferts, and D. Lohse, "Drop impact upon micro- and nanostructured superhydrophobic surfaces," Langmuir (in press).
[42]D. L. Hu, B. Chan, and J. W. M. Bush, "The hydrodynamics of water strider locomotion," Nature (London) **424**, 663 (2003).
[43]D. L. Hu and J. W. M. Bush, "Meniscus-climbing insects," Nature (London) **437**, 733 (2005).
[44]J. W. M. Bush and D. L. Hu, "Walking on water: Biolocomotion at the interface," Annu. Rev. Fluid Mech. **38**, 339 (2006).
[45]E. B. Dussan, "On the spreading of liquids on solid surfaces: Static and dynamic contact lines," Annu. Rev. Fluid Mech. **11**, 371 (1979).

[46]L. M. Hocking, "The motion of a drop on a rigid surface," Proceedings of the Second International Colloquium on Drops and Bubbles, 1982, Paper No. JPL-NASA 82-7, p. 315.
[47]P. D. M. Spelt, "A level-set approach for simulations of flows with multiple moving contact lines with hysteresis," J. Comput. Phys. **207**, 389 (2005).
[48]R. L. Hoffman, "A study of the advancing interface. I. Interface shape in liquid.gas systems," J. Colloid Interface Sci. **50**, 228 (1975).
[49]S. F. Kistler, "Hydrodynamics of wetting," in *Wettability*, edited by J. C. Berg (Dekker, New York, 1993), p. 311.
[50]L. Tanner, "The spreading of silicon oil drops on horizontal surfaces," J. Phys. D **12**, 1473 (1979).
[51]P. Ehrhard and S. H. Davis, "Non-isothermal spreading of liquid drops on horizontal plates," J. Fluid Mech. **229**, 365 (1991).
[52]P. J. Haley and M. J. Miksis, "The effect of the contact line on droplet spreading," J. Fluid Mech. **223**, 57 (1991).
[53]Y. D. Shikhmurzaev, "Moving contact lines in liquid/liquid/solid systems," J. Fluid Mech. **334**, 211 (1997).
[54]Y. D. Shikhmurzaev, *Capillary Flows With Forming Interfaces* (Chapman & Hall/CRC, Boca Raton, 2007).
[55]M. Sussman, "An adaptive mesh algorithm for free surface flows in general geometries," in *Adaptive Method of Lines* (Chapman & Hall/CRC, Boca Raton, 2002).
[56]D. Vadillo, "Characterization of hydrodynamics phenomena during drop impact onto different types of substrates," Ph.D. thesis, University Joseph Fourier, 2006.
[57]F. Xiao, Y Honma and T. Kono, "A simple algebraic interface capturing scheme using hyperbolic tangent function," Int. J. Numer. Methods Fluids **48**, 1023 (2005).
[58]K. Yokoi, "Numerical method for complex moving boundary problems in a Cartesian fixed grid," Phys. Rev. E **65**, 055701(R) (2002).
[59]D. Adalsteinsson and J. A. Sethian, "The fast construction of extension velocities in level set methods," J. Comput. Phys. **148**, 2 (1999).
[60]J. Kim and P. Moin, "Applications of a fractional step method to incompressible Navier-Stokes equations," J. Comput. Phys. **59**, 308 (1985).
[61]F. Xiao, X. D. Peng, and X. S. Shen, "A finite-volume grid using multimoments for geostrophic adjustment," Mon. Weather Rev. **134**, 2515 (2006).
[62]H. A. van der Vorst, "Bi-CGSTAB: A fast and smoothly converging variant of Bi-CG for the solution of nonsymmetric linear systems," SIAM (Soc. Ind. Appl. Math.) J. Sci. Stat. Comput. **13**, 631 (1992).
[63]F. H. Harlow and E. Welch, "Numerical calculation of time-dependent viscous incompressible flow of fluids with free surface," Phys. Fluids **8**, 2182 (1965).